



Universiteit Utrecht

Defects in Crystals of Hard Polyhedra

Faculty of Science

MASTER THESIS

Rein Perton

Experimental Physics

Supervisors:

Dr. LAURA FILION

Debye Institute for Nanomaterials Science

MARJOLEIN DE JAGER MSc.

Debye Institute for Nanomaterials Science

February 22, 2022

Abstract

In this thesis we study defects in crystals of “hard” polyhedral colloids. Hard colloids have an interaction potential that is infinitely large if particles overlap and zero anywhere else. Effectively, this means hard particles do not interact with each other unless they collide like billiard balls. It has been shown that for certain body-centered cubic (BCC) crystals, and for certain crystals consisting of hard polyhedral particles long-ranged one-dimensional deformations are formed when defects are introduced. In this thesis, we both replicate the crowd- and voidion deformations found in crystals of hard cubes, as well as study the defect behaviour of crystals consisting of Elongated Square Gyrobicupola (ESGB) particles.

We study the defect behaviour through Monte Carlo simulations. First, we determine the phase behaviour by simulating compression and expansion in the NPT ensemble. In the NPT ensemble, the number of particles (N), the pressure (P) and the temperature (T) are fixed. For systems of cubes, the phase behaviour we found agrees very well with previous studies. We then studied the defect behaviour of the systems of cubes and were able to reproduce both the voidion, as well as the crowdion that were observed in previous studies.

During the study of the phase behaviour for ESGB particles, we found that the particles showed excessive rotational movement, indicating it could be a plastic crystal. Further study showed this was indeed the case and the rotations happened according to a specific pattern that can be linked to the geometry of the ESGB particle. We then studied the defect behaviour of vacancies and interstitials within crystals of ESGB particles and found that the deformations caused by these defects both are short-ranged and three-dimensional, denying the possibility of a void- or crowdions to exist within the studied systems. Furthermore, the displacement of the nearest neighbours to the defects in the crystals of ESGB particles did not show clear dependency on density.

Contents

1	Introduction	1
2	Theoretical Background	3
2.1	Hard Colloidal Crystals	3
2.2	Elongated Square Gyrobicupola	5
2.3	Defects within Crystals	6
3	Method	7
3.1	Monte Carlo Simulation	7
3.2	Checking for Overlap	12
4	Results	15
4.1	Hard Cubes	15
4.2	Elongated Square Gyrobicupola	18
5	Conclusion and Outlook	24
	Acknowledgements	25
	References	III

1 Introduction

In this thesis we study the behaviour of deformations in crystals consisting of colloidal particles caused by defects. Colloids are small particles with sizes ranging from several nanometers to a few micrometers. Often, colloids are suspended in a medium. The suspended colloids experience random motion. This random motion is caused by collisions with the solvent molecules and is called *Brownian motion*, after the discoverer Robert Brown [1–3].

Brownian motion allows colloids to arrange themselves into numerous structures, including gases, liquids, glasses and crystals. This process is called *self-assembly*. Self-assembly not only occurs in colloidal systems, but also in atoms and molecules. However, due to the relatively slow movement and large size compared to atoms and molecules, colloids are ideal for studying self-assembly on a single particle level.

Another advantage of colloids over atomic systems is the ability to synthesize colloids in many different shapes, like the pseudocubes, ellipsoids, capsules and peanuts, that Wang *et al.* synthesized in a previous study [4], or the polyhedral particles Vutukuri *et al.* synthesized from spherical colloids [5]. Furthermore, Saraswat *et al.* have shown in a more recent study it is possible to synthesize anisotropic colloidal particles using 2-photon polymerization [6]. Closer to this thesis however, is the work done by Irrgang *et al.* in which they determine the equations of state for hard polyhedron fluids [7].

Varying the shape of the colloids greatly affects the interactions between colloids and can therefore lead to different phase behaviour and different crystal structures. There are many other variables that can contribute to the phase behaviour and the crystal structure. For example, the ionic concentration of the solvent [8], the presence of an external field [9] or the coating of colloids with polymer brushes [10] can all affect the interactions between colloids. However, it is not always straightforward and easy to implement these variables consistently in experiments. Thankfully, classical statistical physics describes colloidal systems very well, making it possible to easily explore different colloidal systems before experimentally verifying the findings.

All these different crystal structures have, in practice, at least one thing in common: they are never perfect. A “perfect crystal” is described by a crystal in which every lattice site is occupied by not more than one particle. If this is not the case, the crystal contains a defect. A very common group of defects are point defects. Point defects are irregularities in a crystal, e.g. an extra added particle on a lattice site or the absence of a particle on a lattice site. Studying these defects and the effect they cause can be tricky at times in three-dimensional crystals. In two-dimensional crystals, it is easier to distinguish the defects and more straightforward to observe their effects compared to defects in three-dimensional crystals. The research into defects within two-dimensional crystals is therefore quite extensive. For example, the diffusion of point defects in crystals of charged colloids has been studied both experimentally [11, 12] as well as through computer simulations [13]. Furthermore, the interaction between point defects [14] and the dynamics of dislocations [15] has also been studied. Despite this extensive research into defects in two-dimensional crystals, defects in three-dimensional crystals remained fairly untouched until relatively recently.

Several three-dimensional crystals that were studied before consist of hard spheres. In face-centered cubic (FCC) crystals of hard spheres close to melting, the point defect concentrations have been studied by Bennet *et al.* [16] and Pronk *et al.* [17]. Other studies investigated the local lattice deformation caused by the defects [18, 19]. The main findings of these studies were that in case of hard spheres, the equilibrium concentrations of point defects are small and the deformations these defects caused were local. This is the main reason defects in three-dimensional crystals were expected to be uninteresting, which caused the lack of studies into different three-dimensional crystals. However, Smalenburg *et al.* recently predicted that for simple cubic crystals of hard cubes these defect concentrations can be as high as 6% [20]. This concentration was later found to also hold for hard slanted cubes [21]. Besides the high concentration of defects, Smalenburg *et al.* also found a one-dimensional deformation, later identified by Van der Meer *et al.* as a voidion [22]. These new findings raised the question whether other non FCC crystals could show interesting defect behaviour as well.

To further contribute to this research, we study the defect behaviour of crystals consisting of hard cubes, and crystals made of *elongated square gyrobicupola* (ESGB) particles. De Graaf *et al.* predicted a crystal structure for ESGB particles that at first glance resembles a BCC crystal [23]. BCC crystals of soft colloids are known to form void- and crowdions [3]. Combined with the symmetric properties the ESGB particle exhibits, the predicted crystal structure was the main reason to study the ESGB particle.

In order to study the defect behaviour of a crystal consisting of ESGB particles, this thesis first aims to reproduce the equation of state and the defect behaviour of cubes to validate the correctness of our simulation code. Once these findings are reproduced, we study the phase behaviour of the ESGB particle to find out what kind of crystal the ESGB particles form. Lastly, we introduce defects into the “perfect crystal” of ESGB particles, so that we can study the deformations.

The remainder of this thesis is arranged as follows. In Chapter 2, we provide more background information on defects and on the exact systems that we study in this thesis. Next, Chapter 3 gives an in-depth description on the methods of simulation used in this thesis. In the penultimate chapter, Chapter 4, we first discuss our results for reproducing the phase and defect behaviour of hard cubes, and secondly, we discuss our findings regarding the phase and defect behaviour of ESGB particles. Lastly, in Chapter 5, we conclude this thesis and provide an outlook to the findings of this thesis.

2 Theoretical Background

This chapter will provide some background information on some of the topics discussed in this thesis. Information about hard colloidal systems and what they are precisely will be given in the first section, Section 2.1. Succeeding this section, Section 2.2 will elaborate on the specific hard polyhedra that were chosen to study in this thesis. Lastly, Section 2.3 will provide more information regarding defects.

2.1 Hard Colloidal Crystals

Colloidal crystals come in many different shapes and sizes. They can contain multiple different particles, different sizes of the same particle, or a mixture of both. They can form different structures, which will be elaborated on later. First, however, one of the most important characteristics of a crystal should be talked about: the potential between the particles.

Hard Particles

The potential between two particles is called the *pair potential*. The phase behaviour of a system depends on the pair potential. The dynamics of a particle are also determined by this pair potential. Examples of well known pair potentials are the Lennard-Jones potential [24, 25], which models soft repulsive and attractive interactions, or Coulomb's law [26], which describes the force between two stationary electrically charged particles.

In this thesis we use a different and simpler, but equally well-known, pair potential namely a hard-core interaction. According to this potential, the particles do not experience any attraction or repulsion, unless they collide. In case of collision, the potential becomes infinite, stopping the particles from overlapping. This potential thus only prevents the particles from overlapping. Particles that follow this potential are called *hard particles*. The *hard potential* mimics exceptionally strong repulsion that atoms experience at extremely close distances, but is also a very good approximation for interactions in several colloidal systems.

The hard potential can be described for any shape of particle as:

$$V = \begin{cases} 0 & \text{if not overlapping,} \\ \infty & \text{if overlapping.} \end{cases} \quad (2.1)$$

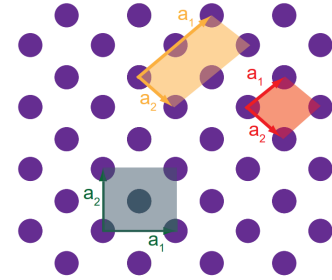
One of the more well known examples of the hard potential is a system of *hard spheres*. For a system of identical hard spheres of diameter σ , Equation (2.1) becomes:

$$V = \begin{cases} 0 & \text{if } r \geq \sigma, \\ \infty & \text{if } r < \sigma, \end{cases} \quad (2.2)$$

with r the center-to-center distance between the two center points of the particles.

Crystal Structures

A perfect crystal can be described by at minimum one pattern or building block that keeps repeating itself. However, more often than not there are multiple different patterns that can make up a single crystal structure. Each one of these patterns is called a *unit cell*. There is, however, one unique type of unit cell containing only one lattice site for each crystal structure. This type of unit cell is called the *primitive unit cell*. A crystal is normally described by primitive unit cells to avoid “duplicates” like in Figure 2.1, where the yellow unit cell is the same as the red primitive unit cell, but repeated in the a_1 direction. The green area shown in Figure 2.1 is a different unit cell than the yellow unit cell. However, the green unit cell is not a primitive unit cell, as it contains more than one lattice point.



One of the most important restrictions on (primitive) unit cells is that they need to be able to tile all of space. This means that they are required to have specific geometries, e.g. a unit cell can never be spherical. It can be shown that these geometries consist of shapes with either 2-fold, 3-fold, 4-fold or 6-fold rotational symmetry. The lattices that obey this requirement can be classified based on the symmetry. These classes are called the Bravais lattices. In 3 dimensions there are in total 14 Bravais lattices, divided in 7 classes (triclinic, monoclinic, orthorhombic, tetragonal, hexagonal, rhombohedral, and cubic)[27]. In this thesis we look at crystals of the cubic class.

Figure 2.1: A schematic preview of two unit cells (yellow and green) and a primitive unit cell (red) in a two dimensional crystal. The axes a_1 and a_2 are the lattice vectors. A linear combination of these vectors is capable of reaching every lattice point in the crystal. Figure taken from Reference [27].

The cubic class consists of three different unit cells, the primitive cubic unit cell, also called the *simple cubic* (SC) unit cell, the *body-centered cubic* (BCC) unit cell and the *face-centered cubic* (FCC) unit cell. Figure 2.2 gives a schematic representation of these three unit cells. The SC unit cell contains 8 octants from 8 different lattice points, totalling to one full lattice point. These octants are placed on the 8 corners of a cube. Both BCC and FCC unit cells build on this SC unit cell. The BCC unit cell, for example, similarly contains 8 octants from 8 different lattice points, placed on the same corners of the cube. However, in addition, it also contains a complete lattice point in the center of the cube. A BCC unit cell thus contains a total of 2 full lattice points. Finally, the FCC unit cell also contains the same 8 octants at the corners of a cube. In addition, the FCC unit cell contains half a lattice point at each face of the unit cell, in the middle of the octants. This totals the final amount of lattice cells in a FCC crystal to 4. These three unit cells all describe different crystal structures. For a hard-sphere system, the maximum packing fractions for these three unit cells differ from approximately 52% for SC to 68% for BCC and 74% for the FCC unit cell. Consequently, at high pressures hard spheres tend to form an FCC crystal. Hard cubes on the other hand do not share this behaviour. Instead, due to their geometry, they tend to form an SC crystal at sufficiently high pressures with a maximum packing fraction of 100%.

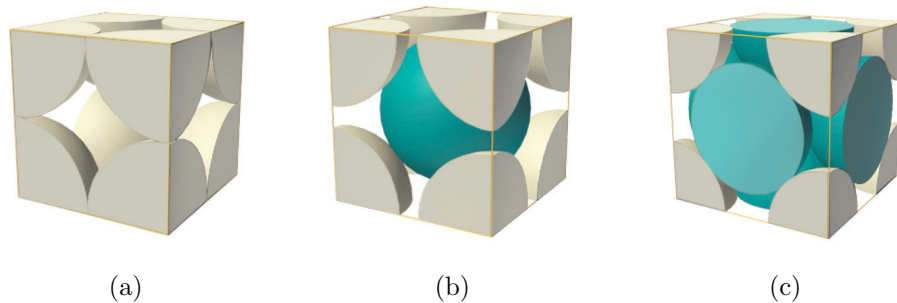


Figure 2.2: Schematic overview of (a) a SC unit cell, (b) a BCC unit cell and (c) a FCC unit cell. Figure taken from Reference [28].

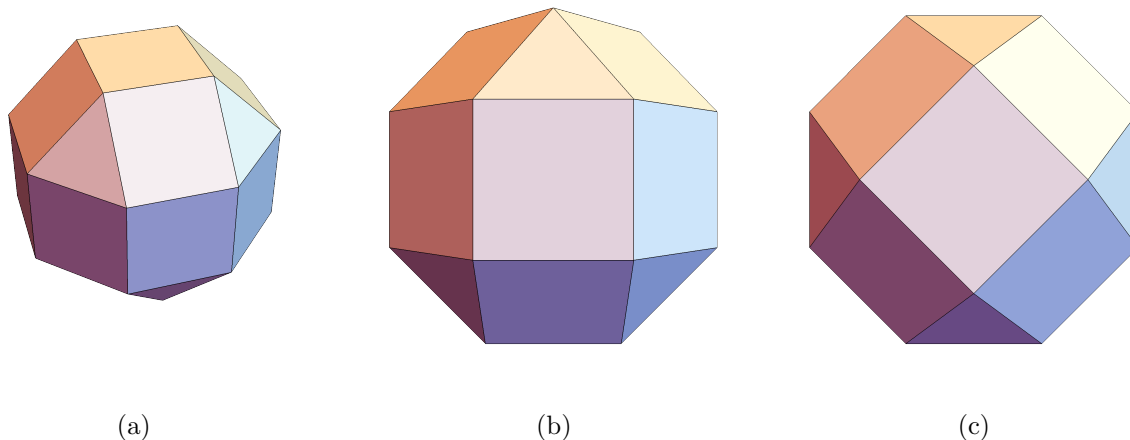


Figure 2.3: Schematic visualization of (a) an ESGB particle, (b) the front view of an ESGB particle (c) the top view of an ESGB particle.

2.2 Elongated Square Gyrobicupola

In this thesis, we will use the well-studied systems of hard spheres and hard cubes to verify that our simulations are running correctly. The actual goal, however, is to study a system of a more exotic particle: the hard elongated square gyrobicupola (ESGB).

The ESGB particle is a convex polyhedron, consisting of a square gyrobicupola that has been elongated by insertion of an octagonal prism between the two halves, see Figure 2.3. In Reference [23] de Graaf *et al.*, predict the densest packed crystal structures of hard polyhedra using a floppy box Monte Carlo. A floppy box Monte Carlo is a Monte Carlo in which the simulation box is allowed to form other shapes than rectangular cuboids [23]. The predicted close packed crystal structure [23] closely resembles a BCC crystal. A BCC structure can be stretched in along its axes. It can be mathematically shown that if a BCC crystal is stretched by a factor $\sqrt{2} \approx 1.41$ along one of its axes, it becomes a FCC crystal. The ESGB unit cell is stretched in the z -direction by a factor of approximately 1.54. That makes the ESGB unit cell officially a FCC crystal instead of the BCC that it at first glance resembles. The maximum packing fraction of the unit cell is approximately 81%. Something worth noting, is the rotational difference between the two particles in the unit cell, Figure 2.4a. The top layer of the unit cell is rotated by 45° around the z -axis with respect to the bottom layer.

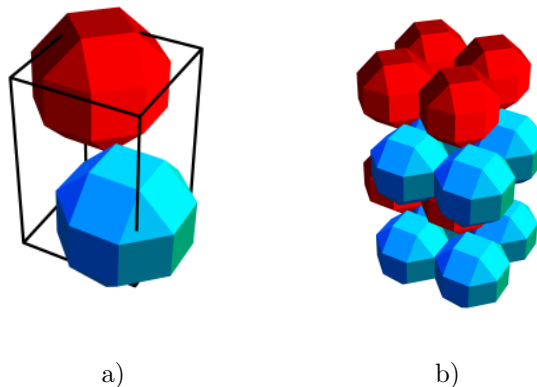


Figure 2.4: a): A schematic view of the densest possible unit cell of the ESGB particle, as predicted by J. de Graaf et al. [23]. b): A schematic view of the densest crystal structure of the ESGB particle, as predicted by J.de Graag et al. [23]. Figures taken from Reference [23].

2.3 Defects within Crystals

As mentioned in the intro, scientists often study “perfect” crystals. However, natural crystals always contain some finite number of defects. There are multiple types of defects, classified by their dimensionality: point, line, surface and volume defects. In this thesis, we focus on point defects. In particular we focus on so-called vacancies and interstitials. A vacancy can be described as a missing particle within the crystal, i.e. a particle is not occupying the lattice site it is supposed to, but instead is missing. Interstitials are the counter to these vacancies, i.e. there is a particle that is occupying the space in between two lattice sites, while the other particles remain at or close to their lattice sites. Figure 2.5 shows a schematic view of these two point defects.

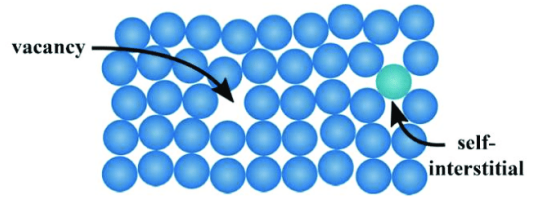


Figure 2.5: Schematic view of the vacancy and interstitial point defects in a crystal structure. Figure taken from Reference [29].

Defects cause deformations in the crystal structure, i.e. the particles will be displaced from their corresponding lattice site. The neighbouring particles of an interstitial, for example, will most likely be pushed away by the interstitial particle. On the other hand, the particles neighbouring a vacancy will most likely move towards the empty space provided by it. These deformations can have a great impact on the electronic, optical and mechanical properties of a crystal. The specific impact or effect, however, depends on the particular shape and range of the deformation. One example of a deformation that could have a substantial impact on the properties of a crystal, is the *crowdion*. Crowdions are one-dimensional, long-ranged deformations caused by interstitials. The crowdion has been proposed by Paneth in 1950 [30]. Though the hypothesis by Paneth was at first contested by Schilling *et al.* [31, 32], the crowdion has since been observed repeatedly, e.g. in BCC crystals of soft repulsive colloids [33, 34]. The shape of the deformation caused by a crowdion can be well approximated by the Frenkel-Kontorova model [35]. The counterpart of the crowdion is the so-called *voidion*, which is a one-dimensional, long-ranged deformation caused by a vacancy. It has been observed in SC crystals of hard cubes, alongside the crowdion [20, 22]. Crowd- and voidion deformations are particularly interesting as they experience extremely low migration barriers and are the most stable form of deformations [36]. Furthermore, studies have shown that these deformations can occur in high concentrations and extend over large areas [20–22, 33, 34]. Figure 2.6 shows the typical deformation caused by a crowd- and a voidion in a crystal of hard cubes.

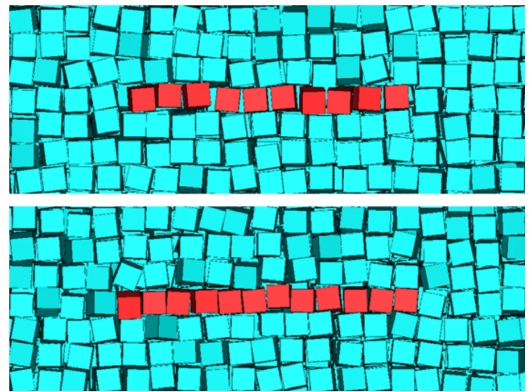


Figure 2.6: The structure of a voidion (top) and a crowdion (bottom) in a crystal of hard cubes. Figure taken from Reference [22].

3 Method

In this thesis we make use of Monte Carlo simulations. In physics, Monte Carlo simulations are often used to simulate problems relating to equilibrium systems that have many coupled degrees of freedom, like fluids, strongly coupled solids, disordered materials and many more. Unlike dynamical simulations, which rely on integrating the equations of motion, Monte Carlo simulations rely on the equilibrium statistics of the system. This makes them ideal for simulating hard particles.

3.1 Monte Carlo Simulation

Monte Carlo Simulations 101

Besides Monte Carlo simulations relying on equilibrium statistics, they have a few more advantages. One of the biggest advantages is that the precision of the results can be easily adjusted, as it does not require an increasingly more difficult approach or calculation to up the precision.

If we consider a system of N particles, each with 3 positional degrees of freedom (e.g. x , y and z), all states can be described by some $3N$ multidimensional space. This space is called *phase space*. Every degree of freedom of each particle adds another dimension to this phase space, e.g. if we add another 2 degrees of freedom for rotation, this multidimensional space would become a $5N$ dimensional phase space. A singular point in phase space is a so-called *microstate* of the system. The evolution of time within the system can then be described by a trajectory of these microstates. A Monte Carlo simulation samples regions of phase space trying to estimate properties of the desired distribution function. Notably, Monte Carlo simulations do not follow the time evolution of the system through phase space, but rather are used to calculate the thermodynamic averages of an equilibrated system.

The process of taking averages is the reason why the precision is easily adjustable. In order to get more precision, more samples of phase space have to be taken. In other words, simply running the simulation for longer will result in more samples of phase space, which in turn will end up improving the precision of the thermodynamic average.

The following explanation of how Monte Carlo simulations work will closely follow References [37] and [38]. We will first need to take a look at some important variables used in Monte Carlo simulations. Normally, the expectation value $\langle Q \rangle$ of an observable quantity Q is calculated by averaging Q over all states μ of the system, weighting each state with their Boltzmann probability

$$\langle Q \rangle = \frac{\sum_{\mu} Q_{\mu} e^{-\beta E_{\mu}}}{\sum_{\mu} e^{-\beta E_{\mu}}}, \quad (3.1)$$

where E_{μ} is the energy corresponding to the state μ , $\beta = 1/k_B T$, with k_B the Boltzmann constant and T the temperature.

This brute force method for calculating expectation values works perfectly fine for systems with a small number of possible states. However, for systems with large numbers of possible states, like continuous systems, this method quickly becomes impractical or even impossible. A solution to this problem is to estimate $\langle Q \rangle$ instead by drawing a subset of M states at random, using some probability distribution p_{μ} , and averaging over those:

$$Q_M = \frac{\sum_{i=1}^M Q_{\mu_i} p_{\mu_i}^{-1} e^{-\beta E_{\mu_i}}}{\sum_{i=1}^M p_{\mu_i}^{-1} e^{-\beta E_{\mu_i}}}, \quad (3.2)$$

where Q_M is the estimated value for $\langle Q \rangle$. One can then increase the precision of the estimation by increasing the number of states M of the subset. Only one problem remains then in order for this method to work for large systems: what is the probability distribution p_μ ?

Choosing p_μ to be equal for all states is the simplest solution. However, it does not solve our problem, but rather brings us back to Equation (3.1), this time taking an average over a subset of the system instead of the complete system. As it turns out, generally, only a small percentage of the total number of states can be sampled. This will often lead to a bad estimator for $\langle Q \rangle$, as the sums in Equation (3.1) may be dominated by a relatively small number of states, which then may not be sampled in Equation (3.2). This phenomenon is predominant at low temperatures, as there is not enough thermal energy for the system to occupy the majority of the states. The system will therefore generally be in close proximity of the ground state, leading to a relatively small number of states dominating $\langle Q \rangle$.

It, thus, becomes important for finding p_μ to know which states contribute most to $\langle Q \rangle$. The technique used for picking these states out of the incredibly large total number of states is called *importance sampling*. This forms the essence of thermal Monte Carlo simulations.

Importance Sampling

As the probability of the system being in a specific state is given by the Boltzmann probability, it is convenient to choose p_μ to be equal to this probability. Therefore, let $p_\mu = Z^{-1}e^{-\beta E_\mu}$, with Z the partition function of the system. This solves the problem of sampling mostly states that are not important, as the probability of all states other than states close to the ground state will have negligible probabilities of being sampled.

If we substitute this probability distribution back into Equation (3.2), the Boltzmann factors cancel one another, and so do the partition functions, leaving us with a simple equation for the estimator

$$Q_M = \frac{1}{M} \sum_{i=1}^M Q_{\mu_i}. \quad (3.3)$$

Now that we have found a convenient method for calculating Q_M , there is one problem that still needs to be addressed: how do we sample the states according to their Boltzmann probability? This is where Monte Carlo simulations rely on *Markov processes* [38].

Markov Processes

A Markov process is a method of generating a random state ν from an initial state μ , with transition probability $P(\mu \rightarrow \nu)$. State ν is random in such a manner, that given the same initial state μ , a Markov process will not generate the exact same state ν every time. There are four constraints on Markov processes. First of all, for a true Markov process, the transition probabilities $P(\mu \rightarrow \nu)$ should not vary over time and should only depend on the properties of state μ , meaning it does not depend on whatever state came before μ . The second constraint is that the transition probability distribution needs to be normalized, thus

$$\sum_{\nu} P(\mu \rightarrow \nu) = 1, \quad (3.4)$$

where \sum_{ν} is the sum over all possible states that can be generated from the state μ .

A Monte Carlo simulation uses these Markov processes in succession. It starts with initial state μ and generates a state ν . This state ν then becomes the initial state, and the Markov process generates a state λ ,

etc. This succession of Markov processes is called a Markov chain. The Markov processes are chosen in such a way that regardless of the initial state of the system, the states produced will appear with probabilities according to the Boltzmann distribution.

The final two conditions that are placed on Markov processes in order to achieve this Markov chain; *ergodicity* and *detailed balance* [37]. Ergodicity tells us that any state in the system must be reachable through a path of non-zero transition probabilities.

Detailed balance is the condition which ensures that the generated system remains in a Boltzmann probability distribution. It does so by adding a constraint to *balance*. Balance states that the average flux of any transition of state μ must be 0, i.e. for every transition $\mu \rightarrow \nu$ there must be a transition $\lambda \rightarrow \mu$ on average. The extra constraint detailed balance then imposes is that for any transition $\mu \rightarrow \nu$, there should on average be a transition $\nu \rightarrow \mu$, reversing the initial transition:

$$p_\mu P(\mu \rightarrow \nu) = p_\nu P(\nu \rightarrow \mu). \quad (3.5)$$

Any transition probability that satisfies this constraint can be used without breaking detailed balance, however, not every transition probability is necessarily equally good. Though there are transition probabilities that tend to work well.

The *Metropolis algorithm* is a well known approach for the transition probability [39]. It is most easily explained if we cut the probability into two terms: i) an acceptance ratio, which determines what transition is chosen, and ii) a transition probability which determines whether the transition is accepted or not;

$$P(\mu \rightarrow \nu) = g(\mu \rightarrow \nu) acc(\mu \rightarrow \nu), \quad (3.6)$$

where $g(\mu \rightarrow \nu)$ is the transition probability of the transition $\mu \rightarrow \nu$ and $acc(\mu \rightarrow \nu)$ the acceptance ratio of the transition.

The acceptance ratio can be anything between 0 and 1. The lower the acceptance ratio chosen, the more likely it is for the system to remain in state μ . This is an unwanted situation, as the system will not be sampled efficiently if the acceptance ratio is too low. One option to solve this problem is by setting $g(\mu \rightarrow \nu)$ to be symmetric, i.e. $g(\mu \rightarrow \nu) = g(\nu \rightarrow \mu)$. This reduces Equation (3.5) to

$$\frac{acc(\mu \rightarrow \nu)}{acc(\nu \rightarrow \mu)} = \frac{p_\nu}{p_\mu}. \quad (3.7)$$

The Metropolis algorithm then chooses to make the acceptance ratio as close to unity as possible by setting the largest of the two to 1, and fixing the other such that Equation (3.7) is still satisfied [40],

$$acc(\mu \rightarrow \nu) = \begin{cases} p_\nu/p_\mu, & \text{if } p_\nu < p_\mu \\ 1, & \text{otherwise} \end{cases}. \quad (3.8)$$

Ensembles in Monte Carlo Simulations

There are multiple ensembles that can be applied to Monte Carlo simulations. One of them is the so called canonical ensemble (NVT ensemble). This ensemble describes systems in which the number of particles is fixed (N), as well as the volume (V) and the temperature (T). The probability of finding the system in a specific state in the NVT ensemble is determined by the Boltzmann factor [41]

$$P(\mathbf{r}^N) = \frac{\exp[-\beta U(\mathbf{r}^N)]}{Z}, \quad (3.9)$$

where \mathbf{r}^N are the coordinates of all particles in that specific state, $U(\mathbf{r}^N)$ the total potential energy of the system in that state and Z the normalization given by

$$Z = \int d\mathbf{r}^N \exp[-\beta U(\mathbf{r}^N)]. \quad (3.10)$$

Substituting Equation (3.9) into Equation (3.8), leaves us with an acceptance probability for NVT systems [38]:

$$acc(\mu \rightarrow \nu) = \begin{cases} \exp[-\beta(U(\mathbf{r}_\nu^N) - U(\mathbf{r}_\mu^N))] & \text{if } U(\mathbf{r}_\nu^N) > U(\mathbf{r}_\mu^N), \\ 1 & \text{otherwise.} \end{cases} \quad (3.11)$$

Aside from the NVT ensemble, there are many other ensembles this acceptance rule can be adjusted to. One of these ensembles used in this thesis is the NPT ensemble, where the number of particles (N), the pressure (P) and the temperature (T) are fixed. The ability for volume changes alters the acceptance ratio from a state μ to a state ν to [38]:

$$acc(\mu \rightarrow \nu) = \min\{\exp[-\beta(U(\mathbf{r}_\nu^N, V_\nu) - U(\mathbf{r}_\mu^N, V_\mu) + P(V_\nu - V_\mu)) + N \log(V_\nu/V_\mu)], 1\}. \quad (3.12)$$

A Complete Trial Move

Having explained the theory behind Monte Carlo simulations, we now turn to the implementation of this theory by going over one entire cycle of our simulation. A cycle is the process that moves the system from one point in phase space to the next. There are multiple ways of defining what happens in a cycle, none of which are wrong. However, some choices are more common than others.

In our case, the choice was made to define a cycle as twice the amount of trial particle moves, i.e. during one cycle $2N$ particles are attempted to either be moved or rotated. This way every particle in the system can theoretically be moved and rotated once during a single cycle. In practice however, this does not happen, as it is randomly chosen which particle's attributes gets changed. In addition, the choice whether a particle is moved or rotated is randomized too. So a random particle gets randomly either moved or rotated. This is all done to make sure that detailed balance is obeyed.

Rotating a particle is done through matrix multiplication. Every particle has a 3×3 matrix, which is used in the simulation for rotating the hard-coded coordinates of the vertices. In order to rotate a particle randomly about any axis, a random unit vector on the surface of a sphere is generated. This assures that any axis is chosen with equal probability, which is needed to obey detailed balance. The only thing that then remains is to translate an angle $\Delta\phi$ about the chosen axis to a rotation matrix that can be multiplied with the existing

rotation matrix. $\Delta\phi$ is chosen randomly in a chosen interval. After the new rotation is done, an overlap check is done. If overlap is found, the rotation matrix is reset and the rotation attempt is rejected.

Volume changes are accepted and rejected according to the *NPT* acceptance rule, Equation (3.12). When a volume change trial move gets past the acceptance rule, one of the axis gets multiplied by a scale factor. It is also a possibility to keep the system in the exact same shape. This could be done by multiplying all axes by a scale factor simultaneously. However, by decoupling the volume changes, our crystal is no longer restricted to the initial configuration of the simulation box. The only things that then remain are to do some bookkeeping and to check if overlap was introduced by the volume change. In coupled volume changes, checking overlap is only necessary when the volume decreases, as when the volume increases, the distances between particles evenly grow. In decoupled volume changes, this is no longer the case, and both for volume increases as well as volume decreases overlap checks need to be done.

Acceptance Ratio's

The movement changes, volume changes and rotations during our simulation all revolve around small adjustments that are chosen randomly. These sizes of the adjustments are important, as it impacts the efficiency of the importance sampling. If the values are too large, hardly any trial moves, rotations, or volume changes will be accepted, and phase space will not be completely explored. However, if the values are too small, the particles move and rotate extremely slowly. This means the system and particles will remain stuck close for a long time to the initial state of the system. Thus, we keep track of how many trial moves, rotations and volume changes are accepted compared to how many are rejected. This ratio is called an *acceptance ratio*. The small adjustments are randomly picked from an interval $[-x,x]$. This interval is based on the acceptance ratio's. We start our simulation with $3 \cdot 10^5$ MC cycles to determine these interval values. Starting with set values, we use the feedback from the acceptance ratio's to increase or decrease these values. It turns out an acceptance ratio's of approximately 30% is ideal [42, 43]. Thus we use intervals of 25% – 35%. If the acceptance ratio's found are higher than 35%, the values are increased,. Vice versa, if the acceptance ratio's that are found are too low, the interval values are decreased.

Periodic Boundary Conditions

Many systems that are studied contain a large number of particles. It would be convenient to study those systems by simulating an incredibly large (more often than not infinitely large) lattice of particles. However, limitations on the size of the simulation are determined by the performance possibilities of modern computers. There is not enough memory or CPU time available to simulate such a large system. The way to get around this is to use *periodic boundary conditions* (PBC's) combined with the nearest-image convention [38]. PBC's can be described by surrounding the system by copies of the system that link back to the system itself. Figure 3.1 shows a 2D example with nearest image interactions. This method can clearly be extended to next-nearest image interactions, or any other form of interactions, though an increase in size of the original system needs to be taken into account as the interaction length increases. As illustrated in Figure 3.1, particle 1 interacts with particle 2 and particle 5, which are located within the boundaries of the system. However, it also interacts with particle 4 and particle 13, both of which lie outside the boundaries. These particles are images of the particles 4 and 13 inside the original system. In other words, images of the system are created by replicating it in every direction. As mentioned before, with longer interaction lengths, the original system will need to be larger, as the interaction length

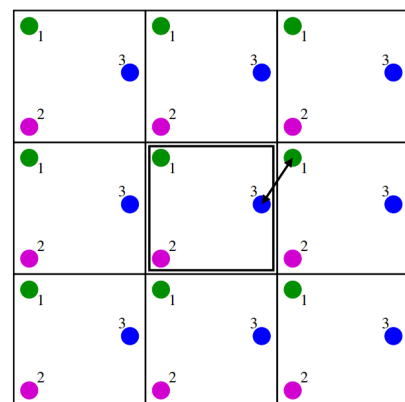


Figure 3.1: Schematic overview of the nearest neighbours across periodic boundary conditions. Particle 1 interacts with particle 3 across the boundary of the system. Figure taken from Reference [44].

should be at most half the system size to avoid interacting with the same particle twice. The interaction length being at most half the system size assures only the nearest image will be taken into account when calculating interactions.

Wigner-Seitz Cell Confinement

The aim of this thesis is to study defect behaviour. Deformations caused by defects have the tendency to migrate through the system, which makes it very hard to study. To prevent this migration of the deformation, we introduce *Wigner-Seitz cell confinement* [17, 45].

A Wigner-Seitz cell is a form of a primitive unit cell that is directly coupled to a lattice point. Wigner-Seitz cells contain all points in space that are closer to the lattice point they are to than any other lattice point [46]. The way this is implemented in the simulation code is by saving the initial lattice sites of all particles. We then make sure the particle cannot move out of the Wigner-Seitz cell, i.e. the initial lattice site needs to remain the closest lattice site to the coupled particle at all times. This is called Wigner-Seitz cell confinement (WS confinement).

By introducing Wigner-Seitz cell confinement into our system, it is assured that all particles in the system are free to move locally, but are globally bound to the initial lattice points they were put onto. This allows for easier study of the deformations introduced by the defects, as the defect and its deformation cannot move throughout the entire system, but are bound to their initial lattice sites.

There is still one problem that needs to be addressed. If we move one particle at a time during the simulation, the center of mass of the system will start to drift. Consequently, the lattice sites will drift along with the center of mass. As the drifted lattice positions move further away from the initial WS positions, the WS confinement is not implemented correctly, and the resulting displacements will be incorrect. To solve this issue, we need to make sure the center of mass location is conserved. This is done by, during the trial move, choosing two particles at random instead of one, and attempting to move them an equal distance in opposite directions. This way, the net displacement of the center of mass is zero.

3.2 Checking for Overlap

As explained in the previous section, the Monte Carlo simulations we use in this thesis rely on certain trial moves, rotations and volume changes. All these trial transformations must be rejected when the transformation creates overlap. Checking overlap for spherical particles is very straight forward: two spheres i and j overlap when $|\mathbf{r}_j - \mathbf{r}_i| < \sigma$, where σ is the diameter of the particles. For the ESGB particle studied in this thesis, however, it is quite complicated.

Polyhedra do not have a radius that describes the center to surface distance for all points on the surface. This is what makes it more complicated. There are multiple methods for collision detection between two non-spherical three dimensional particles, e.g. the Gilbert–Johnson–Keerthi distance algorithm [47], the work that Ming C. Lin did on a variation of the simplex algorithm from linear programming [48] and more. For this thesis, the choice was made to use a method called Separating Axis Theorem (SAT) or Hyperplane Separation Theorem (HST) together with some optimisations to reduce simulation time.

Separating Axis Theorem

Separating Axis Theorem (SAT) is a method of finding overlap between two convex objects [49]. It is based on the principle that if there is an axis on which the objects can be projected such that the projections do not overlap, a separation line can be drawn orthogonal to the axis separating the objects, proving the two objects do not overlap. SAT can be used in 2D as well as 3D.

In principle, an infinite number of lines, or in the case of 3D planes, could be checked before a separation axis is found, if one is ever found at all. This would render SAT useless if this were the case. Fortunately however, it turns out there is a maximum amount of axes that need to be checked to assure overlap or lack thereof.

In 2D the only thing that needs to be checked is whether or not a vertex penetrates an edge of the other object. Therefore the only axes that need to be checked are the normals of the two convex polyhedra. If it is not possible to find a separation axis among these axes, it is not possible at all.

However, in 3D things become a bit more difficult, as checking the particle's normals is no longer enough. As lines become planes in 3D, the edges become faces. Therefore the normal-axes in 3D provide information on whether a vertex penetrates a face. Besides the faces and vertices, 3D polyhedra need to be checked for edge-edge interactions. This is done through the addition of the cross-products between all individual edges of the two polyhedra. To clarify, suppose you have two polyhedra (A and B), with edges (EX and EY), the extra axes that are added to check for overlap in 3D are $AE1 \times BE1$, $AE1 \times BE2$, ..., $AEX \times BEY$.

Optimizations to using SAT

SAT is a good way of finding overlap in 3D, however, there are a few problems. In order for SAT to conclude that there is overlap between two polyhedra, it has to check all of the axes named above. For simple polyhedron shapes with a low number of vertices, this is not a problem. However, as the shapes become more complex with more vertices, the number of axes that need to be checked in case of overlap between two identical polyhedra increases fast. This means that SAT becomes much slower as the polyhedron shape becomes more complicated.

To counteract this, the goal is to minimize the use of SAT while still correctly finding the overlap. The way this is done in this thesis is by implementing smartly chosen center-to-center cutoff distances, for which it can either be concluded that there is or is not overlap without having to use SAT. Hard cutoffs like this are incredibly fast in computing time, especially compared to the more complicated SAT procedure.

The two cutoff distances are based on the inscribed and circumscribed sphere of the convex object. The inscribed sphere is the largest sphere possible to fit inside the polyhedra. The circumscribed sphere is the smallest sphere possible to enclose the entire polyhedra. If the point to point distance between two polyhedra is smaller than twice the radius of the inscribed sphere, there is guaranteed to be overlap. On the other hand, if the point to point distance is larger than twice the radius of the circumscribed sphere, there is guaranteed to be no overlap.

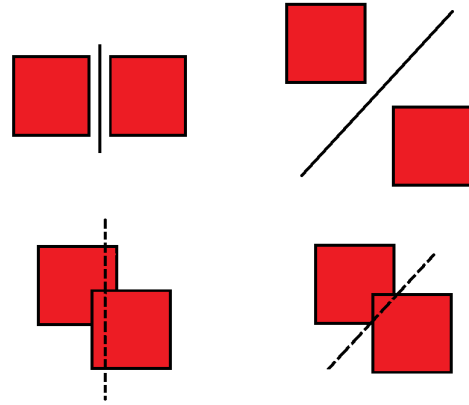


Figure 3.2: The figure above is a schematic of the concept of Separating Axis Theorem. The first row shows how it is possible to draw a separation line between two non-overlapping convex particles. The second row shows that introducing overlap between the particles prevents a separation line from existing.

This way SAT is only used for the intermediate center-to-center distances where the possibility of overlap cannot be determined by considering the center-to-center distance alone. This decreases the simulation time significantly.

Cell listing

Another way of decreasing the simulation time is by implementing cell listing [38]. Cell listing is a method in which you divide the simulation box in squares (2D) or cubes (3D). This way, the center-to-center distance between a particle and all other does not have to be calculated, but can be limited to a particle and all other particles inside its own or neighbouring cells. This reduces a lot of calculations and thus reduces simulation time.

The size of these cells can be variable. There are “soft restrictions” to the cell size however. If they are too large, the effectiveness goes down, as there are more particles inside the cells that are checked for overlap. If they are too small they might not contain all particles that have overlap, meaning there will be overlap in the system without you finding it.

The idea is to calculate the overlap using the methods discussed before within the neighbouring cells instead of the complete simulation box, as for all particles that are not located in the same cell or neighbouring cells there will not be any overlap, thus doing the overlap calculations are redundant and can be skipped. The optimal size of a cell in a *NVT* simulation is therefore equal to the size of a particle. For a *NPT* system, this might not be as straightforward, as the volume of the simulation box is constantly changing. However, it turns out that as long as the number of cells in a particular direction does not change, the particle do not need to be reassigned.

To make life easier, we can also turn the size of the cells into fractional sizes. This means all distances are relative to the box length, e.g. 0 to 1. This way, the size of your cells grows and shrinks with the box size and keeps containing the same particles, as their coordinates are also fractional and change with each volume change. The only thing that needs to be kept track of is the absolute size of the cell after a volume change, as the cell has to at least be larger than the particle size. If the cell shrinks past this limit, the simulation box will have to be redivided into cells that are larger than the particle size, resulting in less cells with more particles inside them.

4 Results

The main aim of this thesis is to study the behaviour of crystals of ESGB particles when point defects are introduced. However, before we do that, we first check that our simulation and analysis code are working correctly by reproducing the equation of state and defect behaviour of hard cubes. These results are discussed in the first section, Section 4.1. Next, in Section 4.2, we turn to the system of ESGB particles. We first compute the equation of state and determine whether the preferred crystal structure at finite pressure is the same as the one predicted by de Graaf *et al.* at infinite pressure [23]. Subsequently, we study the deformation of the found crystal structure caused by a vacancy and an interstitial.

4.1 Hard Cubes

Equation of State

In order to reproduce the equation of state for hard cubes, we run our Monte Carlo simulation with 512 cubical particles of size σ , eight particles in each direction, for various pressures in the NPT ensemble. We start two different runs from two different initial configuration. Our so-called “expansion run” starts off in the perfect crystal configuration at high pressure. The pressure is then slowly lowered, while the packing fraction is monitored. The “compression run” starts off in a fluid configuration. The pressure is then slowly increased, eventually forcing the fluid to become solid. During these runs, the volume changes that occur are coupled, i.e. along all axes the system experiences the same increase or decrease in size simultaneously if the volume change is accepted.

The determination of the equation of state requires particles to move freely throughout the system. This means the Wigner-Seitz cell confinement will not be active at this time. Figure 4.1 shows the simulated data agrees with the data provided by Smallenburg *et al.* [20], showing a fluid phase at pressures lower than $\beta P \sigma^3 \approx 6$, at packing fractions lower than $\eta \approx 0.45$, and a SC crystal at higher pressures. We thus conclude that our simulation is working correctly.

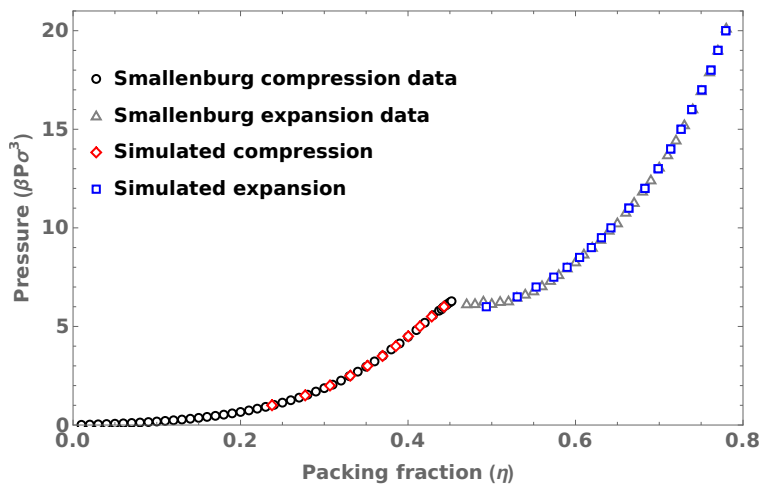


Figure 4.1: Comparison between the equation of state data by Smallenburg *et al.* [20] and the simulated equation of state.

Vacancy

Now that we showed that our simulation code is working correctly, we turn to implementing vacancies and interstitials into the crystal structure and analysing the resulting deformation. As the vacancy is the easiest defect of the two to implement, we start with that one.

We obtain the deformation caused by the vacancy by calculating the average displacement of each hard cube from its corresponding lattice site. Thus, our simulation code is run with a crystal configuration of 512 cubical particles of size σ in the NVT ensemble. This time however, to avoid the deformation caused by the vacancy from migrating across the system, we run the simulation code with Wigner-Seitz confinement active. The vacancy itself is implemented by deleting one particle from the system, making the total number of particles 511. The lattice site it was initially placed on, as well as the Wigner-Seitz cell it was located in, remain part of the system. Figure 4.2 shows the displacement of all particles in terms of the distance between two adjacent lattice points a . The arrows in Figure 4.2 are heavily exaggerated for visual clarity. However, their relative sizes are accurate. The particles of the neighbouring lattice sites all move inwards towards the vacancy, dragging the particles in line with this movement behind them. However, this cannot happen all at the same time. There would not be enough room to crush six cubes inwards into one Wigner-Seitz cell simultaneously.

This is where the orientation of the deformation comes into play. Figure 4.3 shows the distances between two neighbouring particles that lie in the same direction, i.e. the distance between the neighbouring particles in the x -direction, the y -direction or the z -direction, for the first $2 \cdot 10^5$ MC cycles. The grey dots show the three configurations, with 1 being the z -direction, 0.67 the y -direction and 0.33 the x -direction. From Figure 4.3 can be concluded that the orientations observed in Figure 4.2 are alternating, as the displacement of neighbouring particles in the x -direction is never at minimum value when one of the other two directions is, and vice versa. Thus, it must be concluded that the deformation found transitions between these three different orientations, and Figure 4.2 is only part of the story.

In order to determine the average deformation of a single orientation, we make an orientation list. This orientation list is nothing more than an indication of the orientation the system is in, the x -, y - or z -direction.

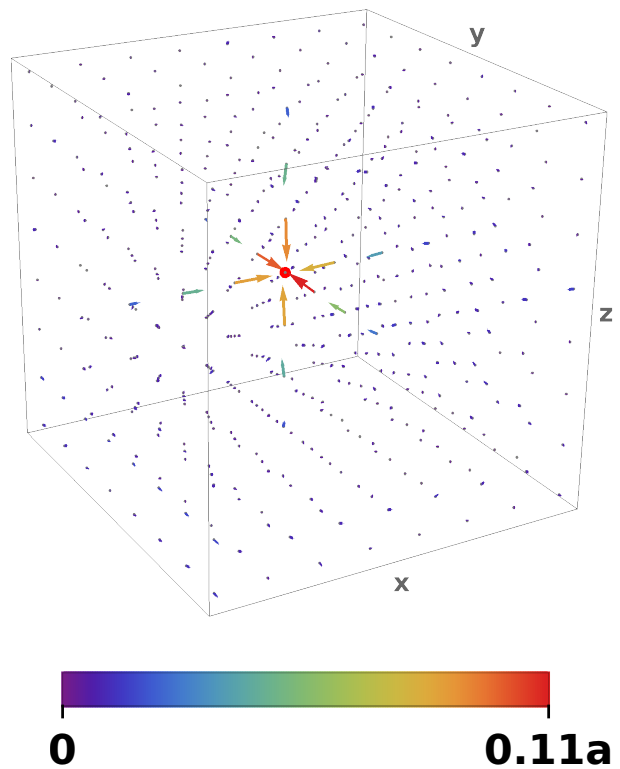


Figure 4.2: The simulated deformation in a SC crystal of cubes caused by a vacancy, without taking the different orientations of the deformation into account.

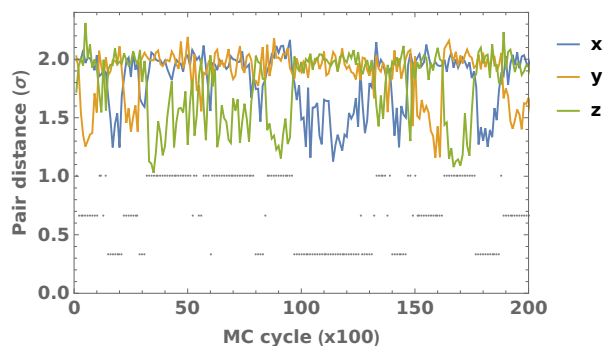


Figure 4.3: The distances between the two nearest neighbours in the x -, y - and z -directions. The gray dots represent the orientation of the deformation based on which nearest neighbour distance is smallest. A value of 1 corresponds to an orientation along the z -axis, a value of 0.67 represents an orientation along the y -axis and a value of 0.33 corresponds to an orientation along the x -axis.

As soon as the orientation of the deformation transitions to a different orientation, the entire system is rotated about the vacancy to match the old orientation to the new orientation before the displacement is measured again. This way, the deformation no longer changes position or rotation, but the system is rotated in such a way that the true displacement of the neighbours can be measured. Note, making the distinction between the three orientations and rotating the system every time the orientation switches is all done in post analyses, not during the simulation.

Figure 4.4 shows the displacement of the system after rotations have been implemented in terms of the distance between two adjacent lattice points a . Notice that the vacancy now causes a one-dimensional deformation, called a voidion, instead of the three-dimensional deformation of Figure 4.2. The initial displacement by the neighbouring particles of the vacancy is relatively large compared to the second and third shell displacements. This falsely suggests that the displacement decays very quickly. However, even the displacement of the third shell of particles still has a significant displacement, making this a long ranged deformation.

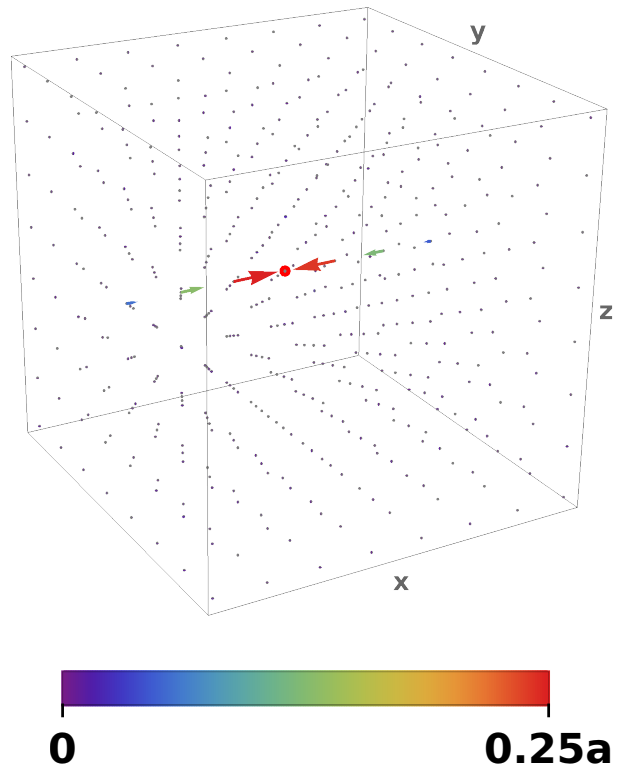


Figure 4.4: The typical deformation caused by a vacancy in a SC crystal of cubes after the deformation rotations have been implemented. The deformation is a long-ranged one-dimensional deformation, also called a void-ion.

Interstitial

Now that we have determined that the vacancy introduces a voidion in a SC crystal of cubes, we look at the defect behaviour an interstitial causes. Similar to the vacancy behaviour, the deformation is obtained by calculating the average displacement of each hard cube from its corresponding lattice site. In order to calculate this displacement, we run our system of 512 cubes of size σ in the NVT ensemble. In similar fashion to the determination of the vacancy behaviour, Wigner-Seitz is used to avoid the interstitial dumbbell from migrating across the system.

The interstitial is implemented by adding a small particle to a chosen Wigner-Seitz cell. The added interstitial particle needs to be small, as we are dealing with hard particles, which cannot overlap. In our case, the interstitial particle has an initial size of 0.05σ . We then, during the simulation, slowly increase the interstitial particle in size until it is of size σ . It is important the interstitial particle is of equal size to the other particles before starting to measure the displacement of all particles, as it otherwise will not show the correct interstitial behaviour. The initial location of the added particle can be important depending on the crystal structure.

However, in case of a SC crystal of cubes, it does not matter, as long as two conditions are met. First, the interstitial must be grown slowly. This will allow the interstitial particle to find the optimal location for it to be in. Second, as is the case with the vacancy behaviour, the deformation caused by the interstitial will have different orientations it can be in. These orientations, need to be dealt with in post analysis. To allow the interstitial particle to get to the most favourable position, the packing fraction should not be too high, as only one orientation will then be allowed.

We chose to put the interstitial particle in the $\langle 111 \rangle$ direction compared to the other particle in the same Wigner-Seitz cell. After we allow the particle to grow to a full sized particle and the system reaches equilibrium, we start the measurements needed to calculate the displacement of all particles. After the different orientations of the deformation are dealt with in a similar fashion to the vacancy behaviour, we are left with the interstitial behaviour shown in Figure 4.5, with a the distance between two adjacent lattice points. The interstitial causes a long-ranged one-dimensional deformation in a SC crystal consisting of cubes. This deformation is also called a crowd-ion.

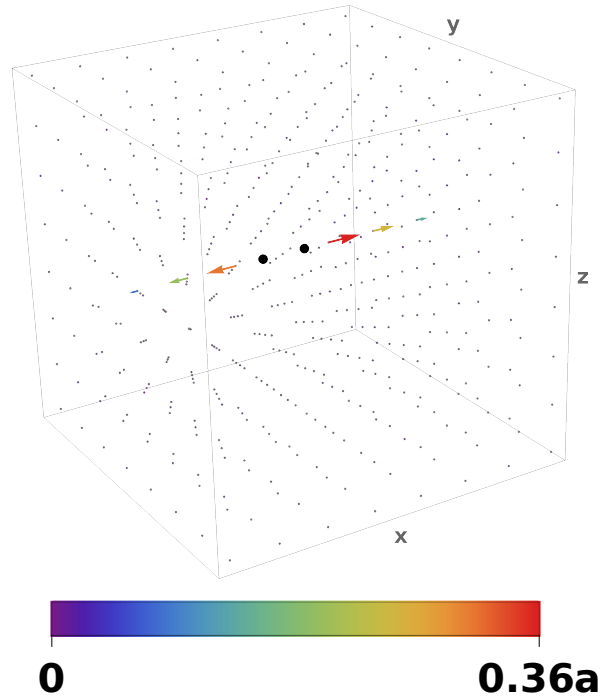


Figure 4.5: The typical deformation caused by an interstitial in a SC crystal of cubes after the deformation rotations have been implemented. The deformation is a long-ranged one-dimensional deformation, also called a crowd-ion.

4.2 Elongated Square Gyrobicupola

Equation of State

Having reproduced the findings for cubes regarding the phase and defect behaviour, it is time to start looking at the ESGB particle. The first step is to find the equation of state, to determine whether the preferred crystal structure at finite pressure is the same as the one predicted by de Graaf *et al.* [23]. Furthermore, determining the equation of state will provide more information on how the crystal behaves at different pressures.

Finding the equation of state is done in the same way as in Section 4.1 for cubes. We run the simulation with a starting configuration of 1400 ESGB particles of size σ . The system is run in the NPT ensemble for different pressures ($\beta P \sigma^3$). Similar to the determination of the equation of state for cubes, we simulate expansion and compression, i.e. we start of with a fluid configuration and gradually increase the pressure and with a perfect crystal configuration of which we gradually lower the pressure. The system is run without Wigner-Seitz confinement, as the particles need to be able to move freely throughout the system. One distinct difference compared to the determination of the equation of states for cubes is the volume changes. In crystals of cubes, these volume changes were coupled. However, as we want to check the preferred crystal structure at finite pressures, we have to make sure the crystal is not forced into a structure it does not want to be in. We do this by decoupling the volume changes, i.e. the volume can increase in either the x-, y-, or z-direction, but not in multiple directions at once. This way, the crystal has the freedom to move into a shape different than the initial configuration.

The average packing density (η) is measured for the different pressures and depicted in Figure 4.6. Figure 4.6 shows both the simulated compression and the simulated expansion. At low pressure ($\beta P \lesssim 0.5$), the simulated expansion is in agreement with the simulated compression. This indicates that both runs are in the same fluid phase. At a pressure of $\beta P \sigma^3 \approx 0.55$, the simulated expansion experiences a phase transition, as it jumps from fluid to solid. This indicates the melting pressure of the system is at approximately $\beta P \sigma^3 \approx 0.55$. Note, in reality, this transition is from solid to fluid, as the simulated expansion starts at high pressure. Between pressures $\beta P \sigma^3 \approx 0.5$ and $\beta P \sigma^3 \approx 1$, a distinct difference can be seen between the simulated compression and expansion. The simulated compression remains in the fluid phase, while the simulated expansion is in the solid phase. The fluid phase that the simulated compression is meta stable. This means the free energy of the crystal phase is lower than the free energy of the fluid phase, however the system cannot transition to a crystal, as it cannot overcome the nucleation barrier. If the pressure is increased even more, eventually, the system will be able to overcome this nucleation barrier, allowing the system to crystallize. We see this happening at $\beta P \sigma^3 \approx 1.1$, where the simulated compression transitions phases from fluid to solid and joins the expansion run. However, if the pressure increases even more, the expansion and compression run separate again. This does not indicate another phase transition. Instead, this can be explained by the inability of the crystal phase to fit properly within the current system configuration.

To find out if the unit cell we found agrees with the unit cell provided by de Graaf *et al.* [23], we look at the ratios of the lattice vectors provided by de Graaf and compare them to the ratios of the lattice vectors we found during our simulation. Figure 4.7 shows the average sizes of a unit cell compared to the size of the unit cell along the x-direction, for different pressures. We conclude that at pressures $\beta P \sigma^3 \approx 0.7$ and higher, the shape of the unit cell stabilizes to a rectangular cuboid, with the x- and y-direction of the unit cell being of equal size and the z-direction approximately 1.42 times as large. The study by de Graaf *et al.* [23] shows this ratio being approximately 1.54. Although the ratios are not exactly the same, they are in reasonable agreement with each other. It is not unexpected for the ratios to be slightly different, as equilibrium values will be different at different finite densities.

Now that the equation of state is known and the crystal structure is reproduced, we can start looking at the defect behaviour. However, during the study of the equation of state, simulation snapshots of the solid phase that were looked at showed a lot of rotational freedom. Therefore, it was decided to study this rotational behaviour of the ESGB particles in the solid phase next.

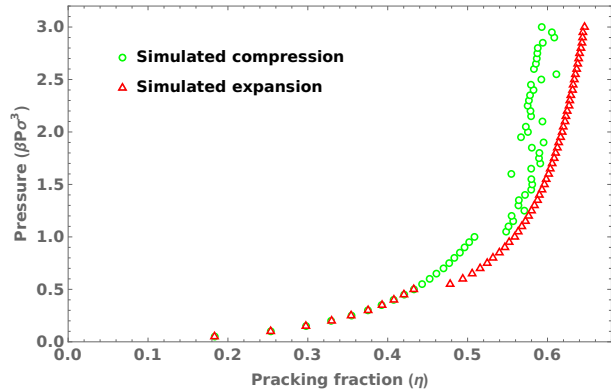


Figure 4.6: The simulated equation of state for a crystal of ESGB particles. One simulation was done compressing a system starting from a fluid phase. A second simulation was done expanding a system starting from a crystal phase.

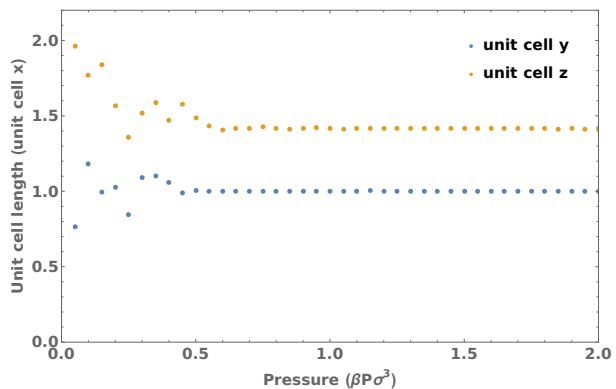


Figure 4.7: The ratio's of the average lengths of the sides of a unit cell in the x-, y- and z-direction compared to the x-direction.

Rotational Preference

As mentioned, the ESGB particles in the crystal show exceeding amounts of rotational movement during the simulation. This is interesting, as it could hint to the crystal of ESGB particles being a *plastic crystal*. Plastic crystals are crystals in which the particles have an orientational degree of freedom.

In order to study this phenomenon, we look at the rotation matrices of the particles. These matrices, when multiplied by a unit vector, provide coordinates that can be transferred to spherical coordinates. These coordinates can then be mapped onto a two-dimensional grid. Once properly normalized, we can make a figure that shows the distribution of the rotated unit vectors. If the unit vectors show rotational preference, then so do the particles.

When it comes to ESGB particles, there is one extra problem that has to be mentioned and taken into account. Figure 2.4 shows both the unit cell and the crystal structure that was predicted by J. de Graaf *et al.* [23]. All blue particles have the same initial rotation matrix. The red particles all have the same rotation matrix as well, however, this rotation matrix is different from the blue particles. It is therefore required to filter the blue particles from the red particles and make sure that for both types of particles, the initial rotation matrix multiplied by a unit vector points in the same direction. Once that is achieved, the previously described steps can be followed, keeping the two different unit vectors for the two different colours in mind.

Figure 4.8 shows the rotational preference of the ESGB particles in the solid phase. At a pressure of $\beta P\sigma^3 = 0.25$, there is no rotational preference, and the particles are free to rotate. This is expected, as the system is in a fluid state at this pressure and there is no form of order in the system, see Figure 4.6. However, as the pressure increases ($\beta P\sigma^3 = 1$), a pattern starts to emerge. This indicates that there is already some form of rotational ordering. This pattern becomes more clear as the pressure increases. At $\theta = \pi/2$ eight peaks in the rotational movement appear. These peaks correspond to the eight faces of the octagonal prism the square gyrobicupola has been elongated with. Out of the eight peaks, four show higher peaks. These can be explained by looking at the peaks located at $\theta = \pi/4$ and $\theta = 3\pi/4$. These peaks correspond to the alignment of the faces of the square gyrobicupola part of the ESGB particle to other particles. It is more favourable to have a rectangular face of one particle lined up with a triangular face of a different particle. This is the case when a particle has a rotated orientation in the xy-plane compared to the initial orientation by $\pi/4 + n \cdot \pi/2$ with n a positive integer. However, if a particle has such an orientation, the surrounding faces are also rectangular, which explains the lower peaks at $\theta = \pi/4$ and $\theta = 3\pi/4$.

With regard to a rotational degree of freedom, it can thus be concluded from Figure 4.8 that the crystal of ESGB particles is indeed a plastic crystal. The crystal of ESGB particles does not have complete rotational freedom, however, there are multiple orientations possible, which the particle can occupy.

Now that we have established the crystal of ESGB particles is a plastic crystal and the phase behaviour of the crystal of ESGB particles is known, it is time to implement the defects and study their behaviour.

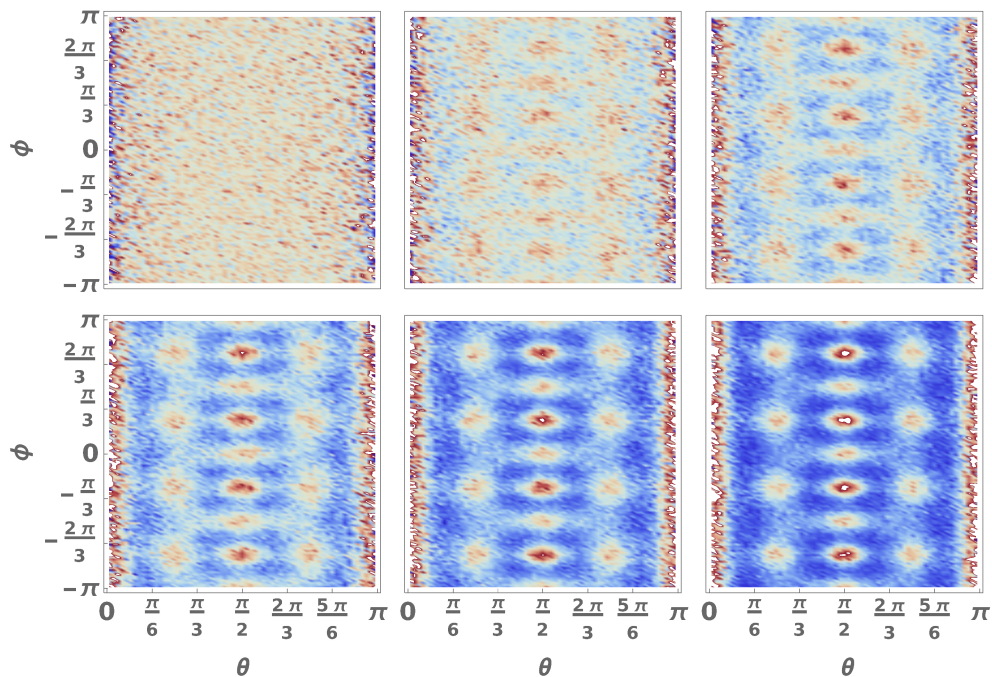


Figure 4.8: The rotational preference of the ESGB particles in a crystal system for the pressures $\beta P\sigma^3 = 0.25$ (top left), $\beta P\sigma^3 = 0.75$ (top middle), $\beta P\sigma^3 = 1.25$ (top right), $\beta P\sigma^3 = 1.75$ (bottom left), $\beta P\sigma^3 = 2.25$ (bottom middle) and $\beta P\sigma^3 = 2.75$ (bottom right).

Vacancy

The vacancy behaviour in the crystal of ESGB particles is found in a similar manner to the vacancy behaviour of crystals consisting of cubes. The simulation code runs a crystal system containing 1400 ESGB particles of size σ in a NVT ensemble. To prevent the vacancy deformation from drifting across the system, we run the simulation code with Wigner-Seitz cell confinement active. The vacancy is implemented by the deletion of a particle. Then, the positions of all particles are saved during the simulation, so that in post analysis, we can calculate the displacement of all particles to their initial lattice point. Figure 4.10 shows this displacement in terms of the distance between two adjacent lattice points (a). The vacancy causes a three-dimensional deformation that is short-ranged. Note that the deformation shows an asymmetric behaviour along the z -axis. The surrounding particles in the xy -plane with $z > 0$ all move inwards towards the vacancy, while the particles with $z < 0$ do not show this behaviour. The reason for this is most likely the difference in orientation between the particles above and below the vacancy.

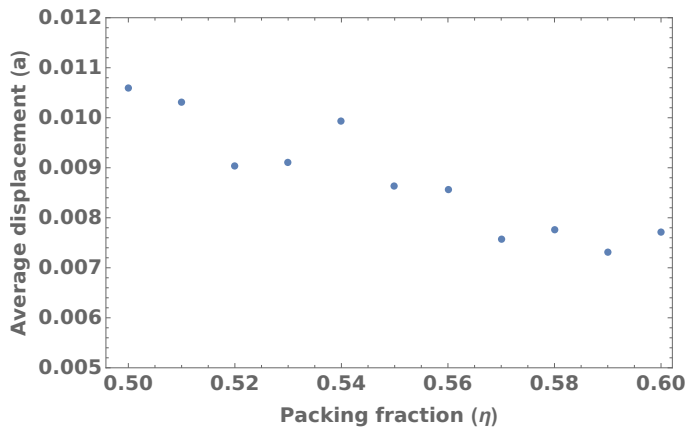


Figure 4.9: The density dependence of the average displacement of the nearest neighbours to the vacancy.

We then looked at the average displacement of the nearest neighbours from their lattice sites at different packing fractions. In order to compare the different displacements, we chose the distance between two adjacent lattice points (a) as the unit of length. This unit scales with the packing fraction. This is important, as in systems with lower densities, there is in general more empty space for particles to move, resulting in larger absolute displacements. Figure 4.9 shows the average displacement as a function of packing fraction. A slight decrease in displacement can be seen for increasing packing fractions. However, this decrease can be considered as a random fluctuation, as the difference between the maximum and minimum displacement is too small, approximately 0.4% of the lattice distance a , to be considered a decreasing trend. We therefore conclude that the average displacement for vacancies in ESGB crystals is not large enough to show any clear dependency on the packing fraction and that in general, the displacement caused by the vacancy is of the order of 1% of the lattice distance (a).

Having determined the vacancy behaviour of the ESGB particles, we now start looking at the interstitial behaviour.

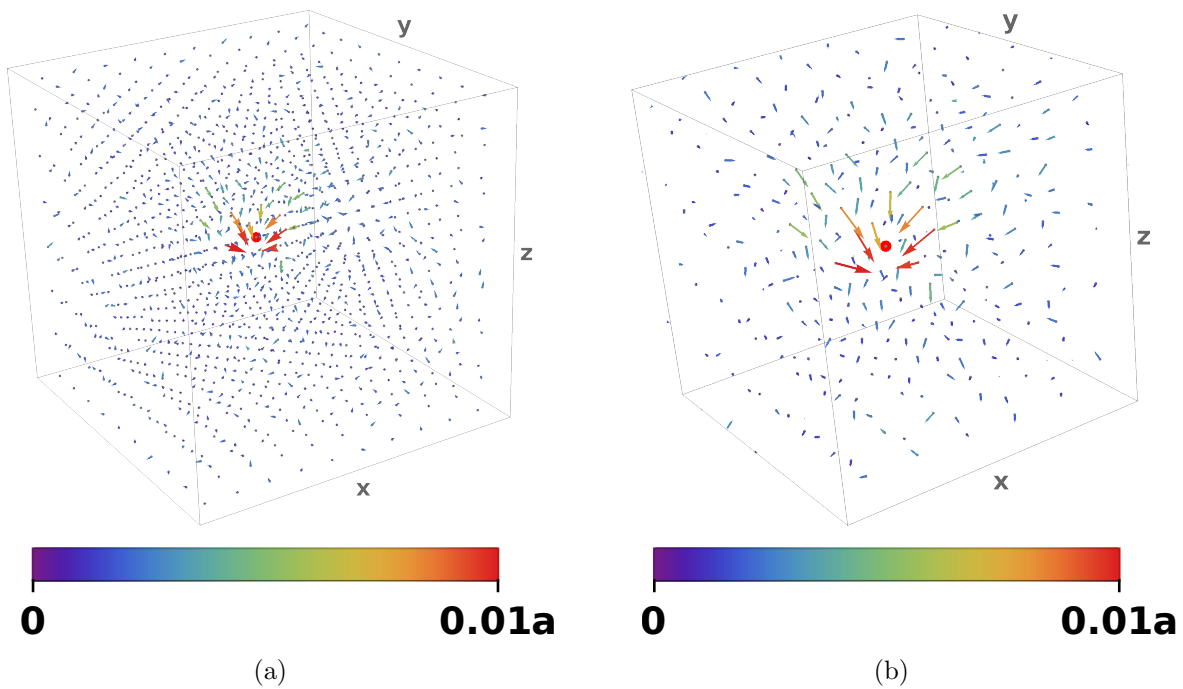


Figure 4.10: (a) The typical deformation caused by a vacancy in a FCC crystal of ESGB particles and (b) a magnification of the deformation. The deformation is a short-ranged three-dimensional deformation, with asymmetric behaviour in the z -direction.

Interstitial

The interstitial deformation in the crystal of ESGB particles is acquired in a similar fashion to the interstitial deformation of the cubes. We run the simulation code in a NVT ensemble, with a system consisting of 1400 ESGB particles of size σ in a crystal configuration. Wigner-Seitz confinement is used in this simulation, as we want to prevent the deformation from migrating across the system. The displacement of particles with respect to their corresponding lattice point is calculated after insertion of an interstitial particle. It is not possible to immediately insert a full sized particle, as the particles have a hard potential. Therefore we are forced to insert a small particle that grows slowly until it is of equal size as the other particles. Figure 4.11 shows the typical displacement caused by the interstitial in terms of the distance between two adjacent lattice points (a). The arrows are exaggerated to improve visual clarity. From Figure 4.11 it can be concluded that the interstitial does not introduce a crowdion in a crystal of ESGB particles. The deformation that is observed is a three-dimensional deformation. The interstitial particle and the particle it shares its Wigner-Seitz cell with are called the *dumbbell couple*. The nearest neighbours of the dumbbell couple move away from the Wigner-Seitz cell the dumbbell couple is located in. These neighbours push away the particles around them, however, this secondary motion is already weak compared to the initial movement. After this next nearest neighbours effect, the repercussions of the interstitial particle are negligible. This means the interstitial causes a deformation that is short range.

We then looked at the average displacement of the nearest neighbours for various packing fractions. Figure 4.12 shows the average displacement as a function of packing fraction. The displacement caused by the interstitial is around 15% of the lattice distance (a). This is roughly a factor 10 larger than the displacement caused by vacancies. The average displacement does not seem to be depending on the packing fraction, but rather fluctuate around a constant value. We thus conclude the average displacement of the nearest neighbours does not depend on the packing fraction.

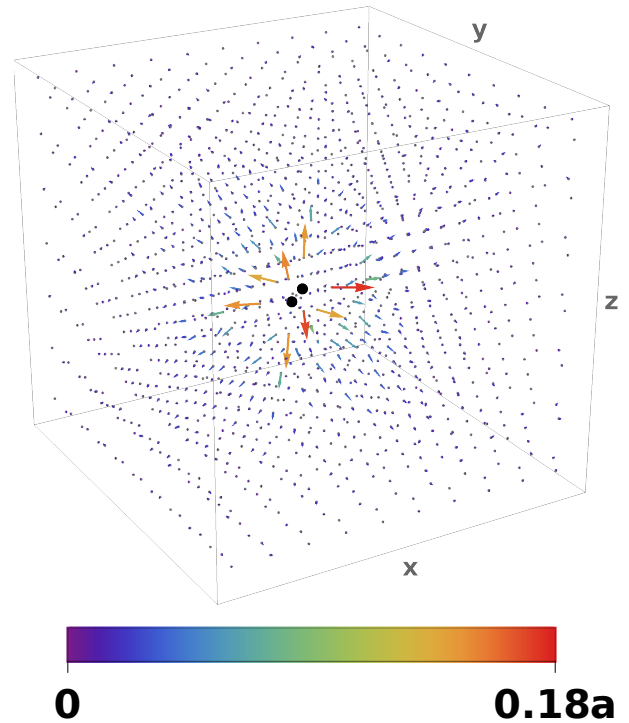


Figure 4.11: The typical deformation caused by an interstitial in a FCC crystal of ESGB particles. The deformation is a short-ranged three-dimensional deformation.

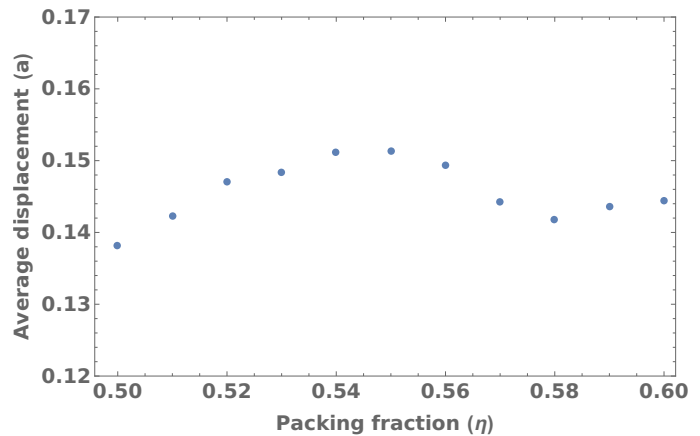


Figure 4.12: The density dependence of the average displacement of the nearest neighbours to the interstitial.

5 Conclusion and Outlook

Ultimately, the aim of this thesis was to study the defect behaviour of a crystal consisting of hard ESGB particles. To achieve this, we first reproduced the phase and defect behaviour of SC crystals consisting of hard cubes to verify that our simulations were running correctly. We found the phase behaviour of these systems to be in good agreement with previous studies by Smallenburg *et al.* [20]. Furthermore, during our study of the defect behaviour, we were successful in reproducing the void- and crowdion that were found in previous studies [22, 32]. We thus concluded that our simulation and analysis code was working correctly.

Next, we studied the phase behaviour of a system of hard ESGB particles. We found that systems of ESGB particles have a fluid phase at pressures lower than $\beta P \sigma^3 \approx 0.55$. The melting pressure of these crystals is located at a pressure of $\beta P \sigma^3 \approx 0.55$. At higher pressures, we found the system transitioned to a crystal phase. After examination of the crystal phase, we concluded that the crystal structure the system formed is a FCC structure, opposed to the stretched BCC structure that was expected from previous work [23].

While studying the phase behaviour of the system, we observed excessive rotational movement, which could indicate that the observed crystal was actually a plastic crystal. However, further investigation in the orientational preference of the particles showed that although the ESGB particles at first seem to rotate freely in the system, they turn out to do so according to a distinct pattern that is coupled to their geometry. This proves that the observed crystal phase is a plastic crystal, as there is a form of rotational freedom.

After we had classified the phase behaviour of ESGB particles, we explored the effect of point defects on the crystal structure. We found that both vacancies as well as interstitials cause local, three-dimensional deformations and do not form the one-dimensional crowd- and voidions. The deformation formed by the interstitial is symmetric. All neighbouring particles are pushed away in the same manner. The vacancy, on the other hand, causes a deformation that is rotationally symmetric in the xy-plane, but asymmetric in the z-direction. The reason for this asymmetric behaviour is not entirely clear. It is likely to be caused by the geometric differences and the difference in orientation of the particles surrounding the vacancy. However, more research is needed to exclude other possible reasons. We have learned that an FCC crystal structure containing ESGB particles does not show any long ranged deformations. However, as BCC crystal structures are known to form crowd- and voidions, more research should be done regarding BCC crystal structures of hard polyhedra.

Acknowledgements

There are many people who helped me during the span of this project. First of all, I would like to thank my daily supervisor Marjolein de Jager for helping me through the rough patches of this thesis and for her insight in condensed matter physics. Secondly, I want to thank my supervisor Laura Filion for her expert opinion on the findings of this research and the opportunity to work on a master thesis under her supervision. Collectively, I would like to thank both the people present at the weekly group meetings for their feedback and help, as well as the people that have taken the time to read through this thesis in search for errors. Furthermore, I want to thank Joost de Graaf for taking the time to be my second examiner. And lastly, I would like to thank my partner for being a patient, listening ear over the past year, even though she does not understand anything I have accomplished in this thesis.

References

- [1] R. Brown, *Xxvii. a brief account of microscopical observations made in the months of june, july and august 1827, on the particles contained in the pollen of plants; and on the general existence of active molecules in organic and inorganic bodies*, The philosophical magazine **4**, 161 (1828).
- [2] L. Filion, R. Ni, D. Frenkel, and M. Dijkstra, *Simulation of nucleation in almost hard-sphere colloids: The discrepancy between experiment and simulation persists*, The Journal of chemical physics **134**, 134901 (2011).
- [3] M. de Jager. *Defects & nucleation in colloidal systems of “soft” particles*. Master’s thesis, University Utrecht, (2020).
- [4] Y. Wang, X. Su, P. Ding, S. Lu, and H. Yu, *Shape-controlled synthesis of hollow silica colloids*, Langmuir **29**, 11575 (2013).
- [5] H. R. Vutukuri, A. Imhof, and A. Van Blaaderen, *Fabrication of polyhedral particles from spherical colloids and their self-assembly into rotator phases*, Angewandte Chemie International Edition **53**, 13830 (2014).
- [6] Y. C. Saraswat, F. Ibis, L. Rossi, L. Sasso, H. B. Eral, and P. Fanzio, *Shape anisotropic colloidal particle fabrication using 2-photon polymerization*, Journal of Colloid and Interface Science **564**, 43 (2020).
- [7] M. E. Irrgang, M. Engel, A. J. Schultz, D. A. Kofke, and S. C. Glotzer, *Virial coefficients and equations of state for hard polyhedron fluids*, Langmuir **33**, 11788 (2017).
- [8] A. Yethiraj and A. van Blaaderen, *A colloidal model system with an interaction tunable from hard sphere to soft and dipolar*, nature **421**, 513 (2003).
- [9] A. Pal, V. Malik, L. He, B. H. Ern e, Y. Yin, W. K. Kegel, and A. V. Petukhov, *Tuning the colloidal crystal structure of magnetic particles by external field*, Angewandte Chemie International Edition **54**, 1803 (2015).
- [10] P. Uhlmann, H. Merlitz, J.-U. Sommer, and M. Stamm, *Polymer brushes for surface tuning*, Macromolecular rapid communications **30**, 732 (2009).
- [11] T. H. Zhang and X. Y. Liu, *Configurations and diffusion of point defects in two-dimensional colloidal crystals*, Applied physics letters **89**, 261914 (2006).
- [12] A. Pertsinidis and X. Ling, *Diffusion of point defects in two-dimensional colloidal crystals*, Nature **413**, 147 (2001).
- [13] A. Libal, C. Reichhardt, and C. O. Reichhardt, *Point-defect dynamics in two-dimensional colloidal crystals*, Physical Review E **75**, 011403 (2007).
- [14] W. Lechner and C. Dellago, *Defect interactions in two-dimensional colloidal crystals: vacancy and interstitial strings*, Soft Matter **5**, 2752 (2009).
- [15] P. Lipowsky, M. J. Bowick, J. H. Meinke, D. R. Nelson, and A. R. Bausch, *Direct visualization of dislocation dynamics in grain-boundary scars*, Nature materials **4**, 407 (2005).
- [16] C. Bennett and B. Alder, *Studies in molecular dynamics. ix. vacancies in hard sphere crystals*, The Journal of Chemical Physics **54**, 4796 (1971).
- [17] S. Pronk and D. Frenkel, *Point defects in hard-sphere crystals*, The Journal of Physical Chemistry B **105**, 6722 (2001).
- [18] N. Y. Lin, M. Bierbaum, P. Schall, J. P. Sethna, and I. Cohen, *Measuring nonlinear stresses generated by defects in 3d colloidal crystals*, Nature materials **15**, 1172 (2016).

- [19] B. VanSaders, J. Dshemuchadse, and S. C. Glotzer, *Strain fields in repulsive colloidal crystals*, Physical Review Materials **2**, 063604 (2018).
- [20] F. Smallenburg, L. Filion, M. Marechal, and M. Dijkstra, *Vacancy-stabilized crystalline order in hard cubes*, Proceedings of the National Academy of Sciences **109**, 17886 (2012).
- [21] R. van Damme, B. van der Meer, J. van den Broeke, F. Smallenburg, and L. Filion, *Phase and vacancy behaviour of hard “slanted” cubes*, The Journal of chemical physics **147**, 124501 (2017).
- [22] B. Van Der Meer, R. Van Damme, M. Dijkstra, F. Smallenburg, and L. Filion, *Revealing a vacancy analog of the crowdion interstitial in simple cubic crystals*, Physical review letters **121**, 258001 (2018).
- [23] J. de Graaf, L. Filion, M. Marechal, R. van Roij, and M. Dijkstra, *Crystal-structure prediction via the floppy-box monte carlo algorithm: Method and application to hard (non) convex particles*, The Journal of chemical physics **137**, 214101 (2012).
- [24] J. E. Lennard-Jones, *On the determination of molecular fields. ii. from the equation of state of gas*, Proc. Roy. Soc. A **106**, 463 (1924).
- [25] J. E. Lennard-Jones, *Cohesion*, Proceedings of the Physical Society (1926-1948) **43**, 461 (1931).
- [26] P. G. Huray, *Maxwell’s equations* (John Wiley & Sons, 2011).
- [27] I. Swart, *Structure of Matter* (Lecture Notes, Utrecht University, 2016).
- [28] H. University. *An arrangement of atoms in crystals*, (2022).
- [29] S. Bellini, Y. Sun, F. Gallucci, and A. Caravella, *Thermodynamic aspects in non-ideal metal membranes for hydrogen purification*, Membranes **8**, 82 (2018).
- [30] H. R. Paneth, *The mechanism of self-diffusion in alkali metals*, Physical Review **80**, 708 (1950).
- [31] W. Schilling, K. Schroeder, and H. Wollenberger, *Three-dimensional versus crowdion migration of interstitials in annealing stage i of irradiated metals*, physica status solidi (b) **38**, 245 (1970).
- [32] P. M. Derlet, D. Nguyen-Manh, and S. Dudarev, *Multiscale modeling of crowdion and vacancy defects in body-centered-cubic transition metals*, Physical Review B **76**, 054107 (2007).
- [33] M. de Jager, J. de Jong, and L. Filion, *Defects in crystals of soft colloidal particles*, Soft Matter (2021).
- [34] R. M. Alkemade, M. de Jager, B. van der Meer, F. Smallenburg, and L. Filion, *Point defects in crystals of charged colloids*, The Journal of Chemical Physics **154**, 164905 (2021).
- [35] J. Koehler, *Crowdions using the frenkel-kontorova model*, Physical Review B **18**, 5333 (1978).
- [36] S. Fitzgerald, *Structure and dynamics of crowdion defects in bcc metals*, Journal of Micromechanics and Molecular Physics **3**, 1840003 (2018).
- [37] M. E. Newman and G. T. Barkema, *Monte Carlo methods in statistical physics* (Clarendon Press, 1999).
- [38] D. Frenkel, B. Smit, and M. A. Ratner, *Understanding molecular simulation: from algorithms to applications* (Academic press San Diego, 1996).
- [39] G. Bhanot, *The metropolis algorithm*, Reports on Progress in Physics **51**, 429 (1988).
- [40] N. Metropolis, A. W. Rosenbluth, M. N. Rosenbluth, A. H. Teller, and E. Teller, *Equation of state calculations by fast computing machines*, The journal of chemical physics **21**, 1087 (1953).
- [41] S. J. Blundell and K. M. Blundell, *Concepts in thermal physics* (Oxford University Press on Demand, 2010).
- [42] B. Jayaram, *On the acceptance ratio in monte carlo computer simulations*, Journal of Mathematical Chemistry **20**, 395 (1996).

-
- [43] D. Frenkel, *Simulations: The dark side*, The European Physical Journal Plus **128**, 1 (2013).
- [44] M. Dijkstra, *Modelling and Simulation* (Lecture Notes, Utrecht University, 2020).
- [45] B. van der Meer, F. Smalenburg, M. Dijkstra, and L. Filion, *High antisite defect concentrations in hard-sphere colloidal laves phases*, Soft Matter **16**, 4155 (2020).
- [46] S. H. Simon, *The Oxford solid state basics* (OUP Oxford, 2013).
- [47] E. G. Gilbert, D. W. Johnson, and S. S. Keerthi, *A fast procedure for computing the distance between complex objects in three-dimensional space*, IEEE Journal on Robotics and Automation **4**, 193 (1988).
- [48] M. C. Lin, *Efficient collision detection for animation and robotics*, Ph.D. thesis, University of California, Department of Electrical Engineering and Computer Science, 1993.
- [49] S. Gottschalk, M. C. Lin, and D. Manocha. *Obbtree: A hierarchical structure for rapid interference detection*. in *Proceedings of the 23rd annual conference on Computer graphics and interactive techniques*, pages 171–180, (1996).